Supplementary material for "A hexagonal Fourier model of grid cells"

Remapping of place fields

In this section, we show how well known remapping phenomena can be understood compactly from the perspective of the hexagonal Fourier framework. In particular, if place cells are spatial-domain and grid cells are frequency-domain functions, then even while grids retain their orientations and spacings (inverse of frequency), changes in phase can easily produce what is termed global remapping. Our formulation is formally quite close to what previous researchers have done; thus novel idea here is expressing this in the Fourier framework.

Here, we do not consider the full relationship between grid and place cells, but rather, a weighted sum of grid fields to produce place fields based on the work of Solstad et al. (2006) in our hexagonal Fourier grid model. We incorporate the grid-cell scale increase by a factor of $\sqrt{2}$ (Stensola et al. 2012), and consider only seven grid modules to produce a Gaussian-like place field. The latter is because Stensola et al. (2012)found five grid modules, but limited sampling in the ventral MEC suggests the possibility of one or two additional grid modules (Ormond & McNaughton, 2015). We considered seven instead of six grid modules, since the largest area covered by tetrodes in the dorsoventral axis in the Stensola et al. (2012)work represents only 50% of the total extent of the axis.

For this, we sum grid field activity from each of seven grid cells at the same orientation and phase and with frequencies 1, 2, 3, 4, 6, 8 and 11 cycles per image (considering the hexagonal region of support), which correspond to $\sqrt{2}$ raised to the power of 1 through 7, respectively, and then rounded to the nearest integer. We set the weight between each grid-to-place-cell connection according to a Gaussian function, similarly to Guanella, Kiper and Verschure (2007), as follows:

$$w_{j,k} = e^{\left(\frac{-\text{dist}\left(\mathbf{p}^{(t)}, \mathbf{d_k}^{(t)}\right)^2_{HEX}}{2s^2} \right)}, \tag{i}$$

where $w_{j,k}$ denotes the weight for the grid cell j to the place cell k, $\mathbf{p}^{(t)}$ denotes the vector with the estimated position of the rat $\left[p_x^{(t)}, p_y^{(t)}\right]^T$ at time t, $\mathbf{d_k}^{(t)}$ denotes the vector with the place cell k spatial offset $\left[d_{k_x}^{(t)}, d_{k_y}^{(t)}\right]^T$ at time t, which can change depending on context, s controls the scale of the place field and $\text{dist}(\mathbf{u}, \mathbf{v})_{HEX}$ denotes the Euclidean distance between vectors $\mathbf{u} = [u_1, u_2]^T$ and $\mathbf{v} = [v_1, v_2]^T$ in hexagonal coordinates, which is defined, similarly to Snyder et al. (1999), as follows:

$$\text{dist}(\mathbf{u}, \mathbf{v})_{HEX} = \sqrt{(u_1 - v_1)^2 + (u_2 - v_2)^2 - (u_1 - v_1)(u_2 - v_2)} \qquad \text{(ii)}$$

The greater the value of s, the wider the place field. The difference from the definition of Snyder et al. (1999) is that they use a "vertical" hexagonal axis at $60°$, whereas we use a "vertical" hexagonal axis at $120°$, meaning that our horizontal component from this axis differs in sign. After applying the weighted sum, a threshold is selected to produce the localized Gaussian-like place field. This threshold is used as a simple way to simulate the idea that a place cell fires only if its summed input is strong enough at a given place at the current context.

The left part of Figure I shows a simple place field generated with a set of seven grid fields at the same phase and orientation with increasing frequency. The unthresholded weighted activity of each grid field is also shown to visualize how each grid cell contributes to the place-field formation. This shows that simple Gaussian-like place fields can be formed with a weighted sum of grid fields at the same phase and orientation, replicating results from Hayman and Jeffery (2008); Solstad et al. (2006).

When all recorded place cells change their response together with changes in the environment, this is known as global remapping; if only some change, this is known as partial remapping (Skaggs & McNaughton, 1998). Remapping can be produced by varying the phases of some of the grid fields considered in the weighted sum, which is conceptually the same as how remapping is computed in the contextual gating hypothesis (Hayman & Jeffery, 2008). Our model offers an additional advantage since it allows one to check how this change in phases affect grid cells both in the Fourier and in the spatial domain, and the corresponding effect on the place fields in the spatial domain. Figure II shows in the left a simple Gaussian-like place field with no phase shift ($\alpha = 0, \beta = 0$) and its corresponding phase-shifted version on the right ($\alpha = 48, \beta = 32$), each showing two grid fields in the frequency and in the spatial domain used as input.

Note in Figure II that the change in the place field location in (G) to the one in (N) is quite noticeable, while the grid fields retain their spacings and orientations. Upon closer inspection, one can see that the grid field phases jump around apparently at random, specially in the Fourier domain, which is expected if the grid cells reflect coefficients of Fourier basis functions. That is, for a change in the location of a place field, the spacings and orientations of the Fourier basis functions of grid fields are fixed, but information of the change is carried within phase (and amplitude), which does change.

In order to build more realistic place fields, we consider four grid phase clusters, as suggested by the findings of Hayman and Jeffery (2008), with seven varying-scale grid fields each as the ones used to produce the simpler Gaussian-like place field shown in the left of Figure I. This allows the simulation of more realistic looking place fields. The right side of Figure I shows a set of such realistic place fields that exhibit partial and global remapping by changing either the phases of the grid cells corresponding to activity from a subset of the place fields, or the phases of all of them, respectively.
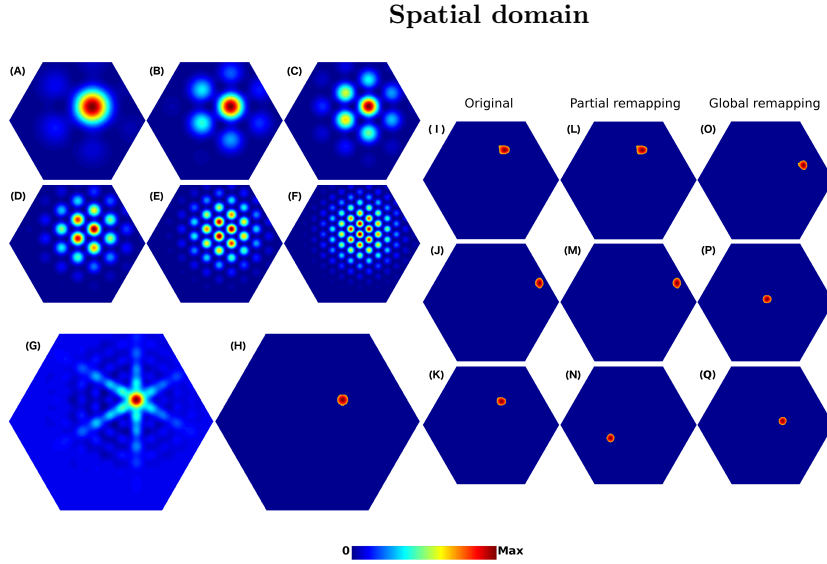
Spatial domain

Figure I: Simulation of different place fields. (A–F) the grid fields used to produce the place fields in (G–H), excluding the one with the lowest frequency for ease of visualization, with respective frequencies 2, 3, 4, 6, 8 and 11 in cycles per image. These frequencies correspond to $\sqrt{2}$ raised to the power of 2 through 7, respectively, then rounded to the nearest integer. The fields are weighted by equation i using the scale parameter $s = 5$ and a common phase shift using $\alpha = 48$ and $\beta = 32$. (G) resultant place field obtained by summing the weighted grid fields in (A–F) plus an an additional weighted grid field of 1 cycle per image (not shown) and then normalizing. The seven grid fields used to produce this place field constitute a grid phase cluster. (H) the same place field as in (G) but thresholded to show only the activity that is equal or above than 2/3 of the maximum. (I–K) Set of three place fields composed each of four grid phase clusters at an initial baseline condition corresponding to an environment. (L–N) partial remapping from the baseline condition, in which only the place field (K) remapped into (N). This corresponds to some hypothetical contextual changes in the same environment as in (I–K). (O–Q) global remapping from the baseline condition, in which all of the place fields changed. This, hypothetically, corresponds to a new environment, different from the one in the baseline condition. All of the grid clusters used have a scale parameter $s = 40$. The colour bar denotes hypothetical average firing rate (arbitrary units).

Derivation of the complex computation equation

The j-th term in the summation on the right hand side of equation 4 is

$$X_{k_1^{(j,\theta)}, k_2^{(j,\theta)}} e^{i\left(u^{(j,\theta)} + v^{(j,\theta)}\right)}.$$
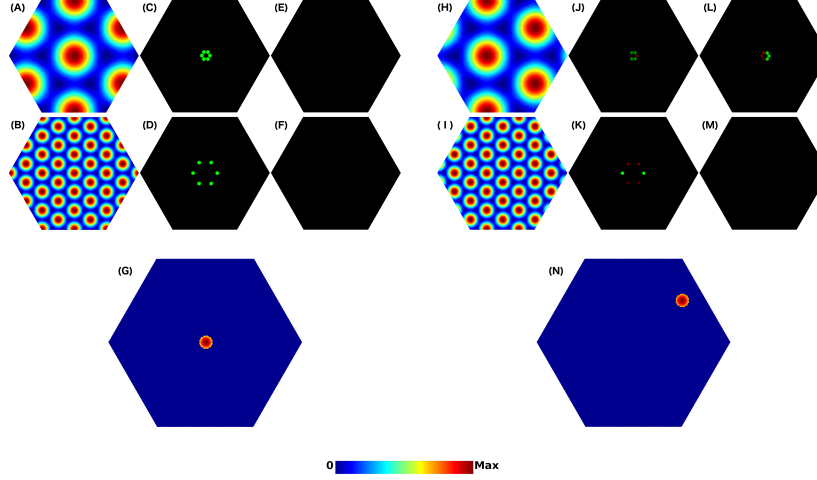
Figure II: Comparison between two simple Gaussian-like place fields with a relative phase shift. (A,B) two out of seven grid fields used to produce the place field in (G), with respective frequencies 2 and 6 in cycles per image. To produce the place field (G), the grid fields are weighted by equation i using the scale parameter $s = 40$ and a common phase shift using $\alpha = 0$ and $\beta = 0$. (C,D) real part of the frequency domain corresponding to (A,B) respectively. (E,F) imaginary part of the frequency domain corresponding to (A,B) respectively. (G) resultant thresholded place field (at 2/3 of the maximum activity) obtained by summing the weighted grid fields in (A,B) plus five additional weighted grid fields (not shown) and then normalizing. (H–N) the same grid fields and place field respectively as in (A–G) but with a common phase shift using $\alpha = 48$ and $\beta = 32$. In the frequency domain, positive values are green, negative red and black indicates zero. The colour bar denotes hypothetical average firing rate (arbitrary units).

Assuming from now on that both j and θ are fixed, and applying Euler's formula, we have

$$X_{k_1,k_2} e^{i(u+v)} = X_{k_1,k_2} \left[\cos(u+v) + i\sin(u+v) \right].$$

Then, applying the identity $\sin(x) = \cos(x - \frac{\pi}{2})$ and then applying equation 6 we have

$$X_{k_1,k_2} e^{i(u+v)} = X_{k_1,k_2} \left[\cos(u+v) + i\cos(u+v-\frac{\pi}{2}) \right] =$$

$$\left[A_{k_1,k_2} e^{-iq} \right] \left[\cos(u+v) + i\cos(u+v-\frac{\pi}{2}) \right],$$

where

$$q = \frac{\pi}{R}\left(\frac{4}{3}\left(\alpha - \frac{1}{2}\beta\right)\left(k_1 - \frac{1}{2}k_2\right) + \beta k_2\right).$$

Then we have

$$X_{k_1,k_2}e^{i(u+v)} = A_{k_1,k_2}\left[\cos(q) - i\cos(q - \frac{\pi}{2})\right]\left[\cos(u+v) + i\cos(u+v - \frac{\pi}{2})\right] =$$

$$\operatorname{Re}\left[A_{k_1,k_2}\left[\cos(q)\cos(u+v) + \cos\left(q - \frac{\pi}{2}\right)\cos\left(u+v - \frac{\pi}{2}\right)\right]\right] +$$

$$\operatorname{Im}\left[A_{k_1,k_2}\left[-\cos\left(q - \frac{\pi}{2}\right)\cos(u+v) + \cos(q)\cos\left(u+v - \frac{\pi}{2}\right)\right]\right],$$

where Re[.] and Im[.] denote the real and imaginary parts respectively. The latter is the definition of equation 10.

Comparison with the Solstad et al. (2006) model

Here we show that the Solstad et al. (2006) model is a special case within the hexagonal grid Fourier model. For simplicity, we consider the case for which both models are at zero phase and $A_{k_1,k_2} = A$ $\forall k_1, k_2$. In our grid-cell model, this corresponds to the case when the exponential shift $X_{k_1^{(j,\theta)}, k_2^{(j,\theta)}}$ becomes a constant A for all parameter values and the imaginary part is zero. Furthermore, by applying Euler's formula $e^{i\theta} = \cos(\theta) + i\sin(\theta)$, equation 4 becomes:

$$x_{r_1,r_2} = \frac{1}{3R^2}\sum_{j=1}^{6} A\left[\cos(u^{(j,\theta)} + v^{(j,\theta)}) + i\sin(u^{(j,\theta)} + v^{(j,\theta)})\right] \quad \text{(iii)}$$

$$\forall \, r_1, r_2 \in \Omega_s.$$

Because of the reflection of the frequency points over the origin in this isotropic scenario (as those depicted in Figure 1B), $k^{(j,\theta)} = -k^{(j+3,\theta)}$ $\forall j = \{1, 2, 3\}$. In addition, because the cosine function is even and the sine function is odd, i.e., $\cos(-\theta) = \cos(\theta)$ and $\sin(-\theta) = -\sin(\theta)$, the imaginary terms in equation iii are zero, giving:

$$x_{r_1,r_2} = \frac{1}{3R^2}\sum_{j=1}^{3} A\left[\cos(u^{(j,\theta)} + v^{(j,\theta)})\right] \quad \text{(iv)}$$

$$\forall \, r_1, r_2 \in \Omega_s.$$

Then, by substituting the value of each frequency point in $\{k^{(j)}\}_{j=1}^{3}$ with the first three in equation 9 (which yield an isotropic grid field):

$$x_{r_1,r_2} = \frac{2A}{3R^2}\left[\cos\left(\frac{\pi\,(2\omega - 0)\,(2r_1 - r_2)}{3R} + \frac{\pi(0)r_2}{R}\right) + \right.$$

$$\cos\left(\frac{\pi\,(2\omega - \omega)\,(2r_1 - r_2)}{3R} + \frac{\pi\omega r_2}{R}\right) +$$

$$\left.\cos\left(\frac{\pi\,(2(0) - \omega)\,(2r_1 - r_2)}{3R} + \frac{\pi\omega r_2}{R}\right)\right] =$$

$$\frac{2A}{3R^2}\left[\cos\left(\begin{bmatrix} \frac{4\pi\omega}{3R} & \frac{-2\pi\omega}{3R} \end{bmatrix}\begin{bmatrix} r_1 \\ r_2 \end{bmatrix}\right) + \right.$$

$$\cos\left(\begin{bmatrix} \frac{2\pi\omega}{3R} & \frac{2\pi\omega}{3R} \end{bmatrix}\begin{bmatrix} r_1 \\ r_2 \end{bmatrix}\right) + \cos\left(\begin{bmatrix} \frac{-2\pi\omega}{3R} & \frac{4\pi\omega}{3R} \end{bmatrix}\begin{bmatrix} r_1 \\ r_2 \end{bmatrix}\right)\right] \qquad \text{(v)}$$

Then, we take the rectangular coordinate equivalent of the previous hexagonal coordinates (see equation 3), yielding:

$$x_{n_1,n_2} = \frac{2A}{3R^2}\left[\cos\left(\begin{bmatrix} \frac{4\pi\omega}{3R} & \frac{-2\pi\omega}{3R} \end{bmatrix}\begin{bmatrix} n_1 + \frac{1}{\sqrt{3}}n_2 \\ \frac{2}{\sqrt{3}}n_2 \end{bmatrix}\right) + \right.$$

$$\cos\left(\begin{bmatrix} \frac{2\pi\omega}{3R} & \frac{2\pi\omega}{3R} \end{bmatrix}\begin{bmatrix} n_1 + \frac{1}{\sqrt{3}}n_2 \\ \frac{2}{\sqrt{3}}n_2 \end{bmatrix}\right) +$$

$$\left.\cos\left(\begin{bmatrix} \frac{-2\pi\omega}{3R} & \frac{4\pi\omega}{3R} \end{bmatrix}\begin{bmatrix} n_1 + \frac{1}{\sqrt{3}}n_2 \\ \frac{2}{\sqrt{3}}n_2 \end{bmatrix}\right)\right] =$$

$$\frac{2A}{3R^2}\left[\vphantom{\begin{bmatrix} n_1 \\ n_2 \end{bmatrix}}\right.$$

$$\cos\left(\begin{bmatrix} \frac{4\pi\omega}{3R} & 0 \end{bmatrix}\begin{bmatrix} n_1 \\ n_2 \end{bmatrix}\right) + \cos\left(\begin{bmatrix} \frac{2\pi\omega}{3R} & \frac{2\pi\omega}{\sqrt{3}R} \end{bmatrix}\begin{bmatrix} n_1 \\ n_2 \end{bmatrix}\right) +$$

$$\left.\cos\left(\begin{bmatrix} \frac{-2\pi\omega}{3R} & \frac{2\pi\omega}{\sqrt{3}R} \end{bmatrix}\begin{bmatrix} n_1 \\ n_2 \end{bmatrix}\right)\right] =$$

$$\frac{2A}{3R^2}\sum_{j=1}^{3}\cos\left(\begin{bmatrix} \frac{4\pi\omega}{3R} & 0 \end{bmatrix}\mathbf{Q}_{\theta+(j-1)\frac{\pi}{3}}\begin{bmatrix} n_1 \\ n_2 \end{bmatrix}\right) \qquad \text{(vi)}$$

$$\forall\, n_1, n_2 \in \mathbb{R}^2$$

where $\theta = 0$ radians (but could be different if the grid pattern needs to be rotated). $\mathbf{Q}_\theta$ is a rotation matrix:

$$\mathbf{Q}_\theta = \begin{bmatrix} \cos(\theta) & -\sin(\theta) \\ \sin(\theta) & \cos(\theta) \end{bmatrix}. \qquad \text{(vii)}$$

Solstad et al.'s sum-of-three cosine function is:

$$\Psi(n_1, n_2) = \frac{1}{3}\left[\sum_{j=1}^{3}\cos\left(k_j\begin{bmatrix} n_1 \\ n_2 \end{bmatrix}\right)\right], \qquad \forall\, n_1, n_2, \qquad \text{(viii)}$$

where

$$k_j = \frac{k}{\sqrt{2}} \left[\cos\left(\theta + \frac{\pi}{12} + (j-1)\frac{4\pi}{12}\right) + \sin\left(\theta + \frac{\pi}{12} + (j-1)\frac{4\pi}{12}\right) \right.,$$
$$\left. \cos\left(\theta + \frac{\pi}{12} + (j-1)\frac{4\pi}{12}\right) - \sin\left(\theta + \frac{\pi}{12} + (j-1)\frac{4\pi}{12}\right) \right].$$

Note that the expression inside each cosine is a scalar $\frac{k}{\sqrt{2}}$ multiplied by a rotation applied to the vector $[n_1\ n_2]^T$. This allows us to reformulate equation viii:

$$\Psi(n_1, n_2) = \frac{1}{3} \left[\sum_{j=1}^{3} \cos\left(\begin{bmatrix} \frac{k}{\sqrt{2}} & \frac{k}{\sqrt{2}} \end{bmatrix} \mathbf{Q}_{\theta' + (\mathbf{j-1})\frac{\pi}{3}} \begin{bmatrix} n_1 \\ n_2 \end{bmatrix} \right) \right] \tag{ix}$$
$$\forall\ n_1, n_2,$$

where $\mathbf{Q}_{\theta'}$ is the rotation matrix from equation vii and $\theta' = \theta + \frac{\pi}{12}$. By setting the frequency component $k = \frac{4\pi\omega}{3R}$, note that the first row vector is rotated $45°$ counterclockwise with respect to the first row vector in equation vi, which is at $0°$. If we instead apply this $45°$ rotation beforehand, we obtain the following:

$$\Psi(n_1, n_2) = \frac{1}{3} \left[\sum_{j=1}^{3} \cos\left(\begin{bmatrix} k & 0 \end{bmatrix} \mathbf{Q}_{\theta + (\mathbf{j-1})\frac{\pi}{3}} \begin{bmatrix} n_1 \\ n_2 \end{bmatrix} \right) \right]. \tag{x}$$

$$\forall\ n_1, n_2$$

Note that the angle θ is already the same as that from equation vi. Then if we set the amplitude $\frac{1}{3} = \frac{2A}{3R^2}$ equation x and equation vi become exactly the same, hence the proof is complete. The Fourier perspective makes it clear that the sum-of-three cosine model does not allow us to see the frequency-domain information, e.g., the imaginary part when there is a phase shift, which could potentially be relevant information for grid cells. We thus conclude that the model from Solstad et al. (2006) is a special case within our hexagonal Fourier model. The hexagonal Fourier model incorporates the sum-of-three model but generalizes it.

	ES		LS	
Base	Mean	S.D.	Mean	S.D.
$\sqrt{2}$	0.835	0.090	0.258	0.063
2	0.815	0.101	0.152	0.045
$\sqrt{2}^3$	0.787	0.105	0.102	0.033
e	0.796	0.103	0.119	0.038
4	0.492	0.075	0.074	0.025

Table A: Mean and standard devation (S.D.) of correlation coefficient of 100 natural images after filtering in the frequency domain with either exponential sampling (ES) or linear sampling (LS) and applying the inverse HDFT. For each row corresponding to a particular exponential base for the ES filter (which was used in order to set the exact same number of grid cells in the LS filter) the largest mean correlation is highlighted in yellow.

	ES		LS	
Base	Mean	S.D.	Mean	S.D.
$\sqrt{2}$	0.144	0.002	0.170	0.003
2	0.104	0.003	0.114	0.002
$\sqrt{2}^3$	0.092	0.002	0.097	0.003
e	0.091	0.003	0.097	0.002
4	0.082	0.004	0.080	0.005

Table B: Mean and standard devation (S.D.) of correlation coefficient of 10 white noise images after filtering in the frequency domain with either exponential sampling (ES) or linear sampling (LS) and applying the inverse HDFT. For each row corresponding to a particular exponential base for the ES filter (which was used in order to set the exact same number of grid cells in the LS filter) the largest mean correlation is highlighted in yellow. Note that there is no noticeable advantage with any exponential base as can be seen more clearly in Figure 5B.